Research Article

Yaoguang Huang*, Aining Zhao, Tianjun Zhang, and Weibin Guo

Plastic failure zone characteristics and stability control technology of roadway in the fault area under non-uniformly high geostress: A case study from Yuandian Coal Mine in Northern Anhui Province, China

Abstract: In order to explore the effective support method for deep broken roadway, based on the *in situ* stress test results, the analytical and numerical solutions of the stress and the range of plastic failure zone (PFZ) in a circular roadway subjected to non-uniform loads were obtained using analytical and finite difference numerical methods based on the elastoplastic theory, respectively. Their comparison results show that the analytical and numerical methods are correct and reasonable. Furthermore, the high geostress causes the stress and range of PFZ in roadway roof and floor to increase sharply while those in roadway ribs decrease. Moreover, the greater the difference of horizontal geostress in different horizontal directions is, the larger the range of PFZ in roadway roof and floor is. The shape of PFZ in roadway varies with the ratio of horizontal lateral pressure coefficient in *x*-direction and *y*-direction. Finally, according to the distribution characteristics of PFZ and range of PFZ under the non-uniformly high geostress, this paper has proposed a combined support scheme, and refined and optimized supporting parameters. The field monitoring results prove that the roadway deformation and fracture have been effectively controlled. The research results of this paper can provide theoretical foundation as well as technical reference for the stability control of deep broken roadway under non-uniformly high geostress.

1 Introduction

Faced with the current predicament of the depletion of shallow mineral resources, many coal mines (mining depth is up to 1,500 m) and mines of metal ores (mining depth is up to 4,500 m) have to enter the stage of deep mineral extraction [1,2], which has brought a lot of new problems and challenges. Under the strong influence of "three high and one disturbance-high geostress, high ground temperature, high karst water pressure, and mining disturbance", the roadway surrounding rocks have the salient features of large deformation, strong rheology, high instability, and extreme difficulty in supporting control [2–5]. Among them, the high geostress and complicated geological structure framework are the key factors that cause these problems. As regards the high geostress, Li et al. [6], Liu et al. [7], and Liu et al. [8] pointed out that the geostress has extremely strong directional characteristics in China by analyzing vast amounts of geostress data from *in situ* tests. The lateral pressure coefficient (stress ratio of between maximum horizontal and vertical) is 0.85–2.63, while the ratio of maximum horizontal principal stress to minimum principal stress is 0.6–2.02. Therefore, it is the foundation of maintaining the stability of deep roadway to grasp the deformation and fracture law of surrounding rock under high, especially non-uniform geostress.

Aiming at this problem, Park and Kim [9] obtained the complete stress–strain solution of the circular roadway subjected to uniform (i.e., horizontal stresses are evenly distributed and equal to vertical and can be different in each horizontal direction) loading conditions based on different deformation criteria in an elasto-plastic zone and elastic–brittle criterion. Sharan [10,11] also obtained the stress fields and displacement fields in

* Corresponding author: Yaoguang Huang, College of Sciences, Center for Post-Doctoral Studies in Safety Science and Engineering, Xi'an University of Science and Technology, Xi'an 710054, Shaanxi, China, e-mail: hyg85@xust.edu.cn
Aining Zhao, Tianjun Zhang: College of Sciences, Xi'an University of Science and Technology, Xi'an 710054, Shaanxi, China
Weibin Guo: College of Energy Engineering, Key Laboratory of Western Mine Exploitation and Hazard Prevention with Ministry of Education, Xi'an University of Science and Technology, Xi'an 710054, Shaanxi, China

surrounding rocks by using Hoek–Brown's elastic–brittle criterion. Fahimifar and Hedayat [12] determined the stress states and displacement fields in the rock masses around axisymmetrical excavating circular opening by assuming that all the strength parameters are linear functions with plastic shear strain. In addition, under the assumption of the "Three-zones failure model (i.e., failure zone, plastic zone and elastic zone)" of the roadway, Jiang et al. [13] not only concluded the closed analytical solutions of stresses and deformation by taking advantage of the Mohr–Coulomb criterion and non-correlated elastoplastic method, but also obtained the calculation formulas of the extent of fracture zone and plastic zone in the roadway. These results have laid a theoretical foundation for studying roadway deformation and failure. However, since these researches on roadway deformation and failure are only carried out under uniform loads, their results cannot be used to study the roadway deformation and failure under deep and non-uniformly high geostress. Therefore, Sun and Lu [14] and Pan et al. [15] deduced approximate analytical solutions of stress, displacement, and radius in the elastic zone, plastic softening zone, and plastic residual fracture zone of circular roadway under non-uniform (i.e., horizontal stresses are evenly distributed but different than vertical) loads based on the trilinear stress–strain softening model and plastic flow theory, which lays a theoretical basis for studying the deformation and fracture law of roadway under deep and high geostress. On this basis, Li et al. [16] discussed the shape and type of plastic zone in a rectangular roadway with variable spans under different lateral pressure coefficients by employing Fast Lagrangian Analysis of Continua in 3 Dimensions (FLAC[3D]). Ma et al. [17] researched the distribution regularity of plastic zone in roadway under different support schemes with a horizontal lateral pressure coefficient of 0.75. Besides, Huang et al. [18] and Xiao et al. [19], Gao et al. [20] and Yu et al. [21] and Lin et al. [22] studied the roadway deformation and fracture under different lateral pressure coefficients based on the finite element method (for example, ADINA-Automatic Dynamic Incremental Nonlinear Analysis, COMSOL Multiphysics) and the discrete element method (for example, UDEC-Universal Distinct Element Code, PFC-Particle Flow Code), respectively, which provided a numerical simulation reference for the roadway support with non-uniform loads.

On the basis of the results of the above studies, Wang et al. [23] proposed a full-section bolt-grouting-reinforcement technology for the surrounding rock of loosely fractured roadway under uniform load, while Cao et al. [24] enriched and improved this technology and optimized its support parameters to make it suitable for an extremely fractured roadway. He and Zhang [4] discovered that the extent of damage to surrounding rocks of the roof and floor increased proportionally to the lateral pressure coefficient under high-level tectonic stress, so they proposed a combined control scheme of "high strength high pre-tension long bolt + large diameter high strength anchor cable + yieldable U-shaped steel support + grouting behind the roadway ribs". Moreover, Cao and Li [5] further pointed out that there is a nonlinear positive correlation between roof–floor deformation and lateral pressure coefficients, and proposed a scheme of combined arch–beam and support. Zhang et al. [25] put forward the use of reinforced concrete to support and control roadway under the deep and high *in situ* stress roadway. Furthermore, Duan et al. [26] and Feng et al. [27] proposed the idea and method of stability control through *in situ* observation and mechanism analysis of damage fracture of surrounding rock of large chamber under high geostress, making it more targeted and reasonable. The results of the above studies help to open up new concepts and methods for roadway deformation and fracture and support under deep and high geostress. However, these researchers only considered the condition that the maximum horizontal geostress is not equal to the vertical stress, but ignored the influence of non-uniformity of horizontal geostress in different horizontal directions on the roadway deformation and failure, as well as the design and parameter optimization for roadway support, such as length, spacing, row spacing, and arrangement of grouting bolt or cable and so on.

Therefore, in order to acquire the influence of law of the difference of horizontal geostress in different directions on the roadway failure, this paper first uses the elastoplastic theory to derive analytical solutions of the stress and range of PFZ in the surrounding rock under non-uniform geostress, and compares the analytical solutions with numerical solutions obtained by FLAC[3D] software. Second, the numerical simulation method is used to obtain the stress fields, the distribution characteristics, and the range of PFZ in the roadway surrounding rock under high and non-uniformly horizontal geostress (i.e., horizontal stresses are evenly distributed but different than vertical and can be different in each horizontal direction). Finally, a combined support scheme for the roadway in the fault tectonic area under high and non-uniform geostress is proposed, based on the numerical results. The support parameters of this combined support are optimized, and the deformation characteristics of

roadway are monitored on site. These research methods and results in this paper can provide the basic theory, data reference as well as methodological reference for the stability control of the deep fractured roadway.

2 General situation of engineering geology and *in situ* stress

2.1 Engineering geology background

Yuandian Coal Mine is located in the junction of Suixi County and Guoyang County (Figure 1), Anhui Province, China. It is west to Yuandian Fault as the boundary, east to –1,000 m horizontal projection line of 10# coal seam, south to WuGou–YangLiu Fault (adjacent to the WuGou Coal Mine), and north to ZhangYouFang Coal Mine, as shown in Figure 2. The whole mining area is located at the southern end of the Xusu arc-shaped fault structure. Its tectonic framework is controlled by nearly EW and NE trending and Xusu arc-shaped fault structure. There are many faults and strong geological structure in the mine field.

At present, the 10# coal seams of the No. 105 mining area are planning to be mined in this mining area, with a depth of between –600 and –950 m. The southern end of the mining area is mainly controlled by the Wugou–YangLiu fault with an inclination angle of between 65° and 75°, and the throw is within 178–340 m. While the northern end is mainly blocked by the coal pillar of F1 fault with an inclination angle of between 50° and 70° and a throw of 300–500 m. The survey suggests that 16 faults have been

exposed in the mining area, all of which are normal faults with an inclination angle of between 50° and 70° and a throw of less than 30 m, and belong to small faults. In addition, the strata in the mining area are relatively complex with diversified variety of rock layers and different thicknesses, and are generally unevenly distributed. However, the dip angle of formation is relatively flat, and the average inclination angle is about 8°, as shown in Figure 2. These signify that this mining area under the influence of a large number of fault structures and complex rock formations has high and complicated geostress, which will cause the deformation and failure characteristics of the surrounding rock to be seriously affected, and thus affect the stability of the excavating roadway in the mining area (see Figure 2).

2.2 Characteristics of *in situ* stress

In order to obtain the geostress in the No. 105 mining area, the borehole stress-relief method (its detailed test principles and methods can be referred to in ref. [28,29]) is used to measure the *in situ* stress at two measuring points in the mining area adjacent to the No. 105 mining area. Figure 2 shows the measurement points and directions of *in situ* stress, and Table 1 shows test results of *in situ* stress in the mining area. It is shown from Table 1 that the medium principal stress in this region is approximately equal to the vertical stress (i.e., overburden gravity); both the maximum and minimum principal stresses are horizontal stresses because they have an inclination of less than 10°, but the stress ratio between the maximum and minimum principal is 1.88–2.09, which
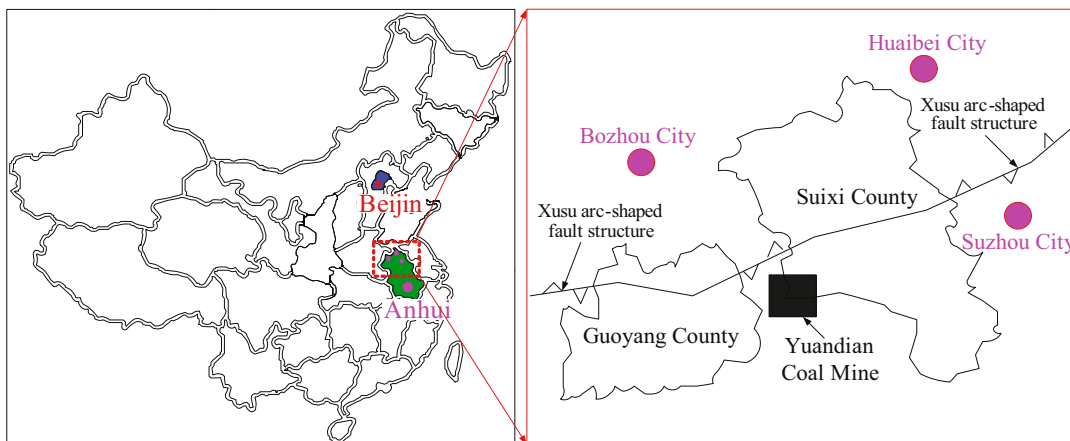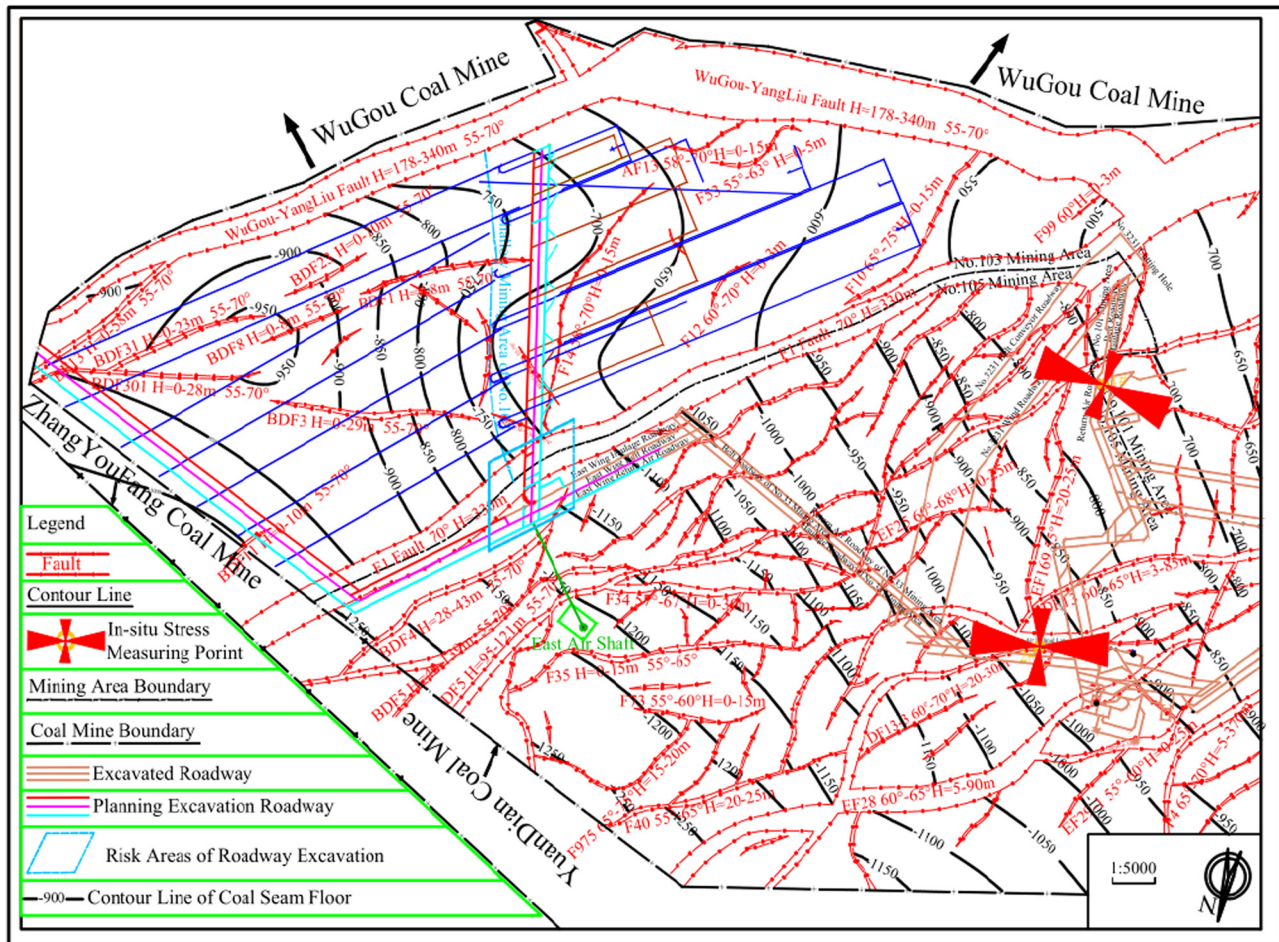

Figure 1: The location diagram of the Yuandian Coal Mine.

Figure 2: Distribution characteristics of the geological structure and *in situ* stress in mining area.

Table 1: Field test results of *in situ* stress

No.	Buried depth h (m)	Stress	Value (MPa)	Azimuthal angle (°)	Dip angle (°)	Lateral pressure coefficient λ
1#	−773	σ_1	26.04	91.36	2.36	1.35
		σ_2	19.22	78.71	83.29	
		σ_3	12.48	178.32	8.93	
		σ_V	19.33	90.00	90.00	
2#	−772	σ_1	26.25	88.25	9.73	1.36
		σ_2	19.36	78.71	83.29	
		σ_3	14.00	176.66	7.34	
		σ_V	19.30	90.00	90.00	

Note: σ_1, σ_2, and σ_3 are the maximum, medium, and minimum principal stresses, respectively; σ_V is the vertical stress.

has strong directional characteristics; the lateral pressure coefficient is approximately 1.35. All of these will strongly affect the characteristics of roadway deformation and failure and its stability after excavation.

As these three mining roadways planned to be excavated will run through the F1 fault in the mining area (Figure 2), it becomes a dangerous area for excavating roadway after considering the effect of the high geostress in the area, complex geological stratum occurrence environment, low strength, and large deformation characteristics of the faulted rock mass inside the F1 fault. Therefore, the deformation and failure characteristics of the roadway under non-uniformly high geostress in the large fault structure area can be

obtained. Which can not only offer basic theoretical support for the excavation and reinforcement design of the roadway, but also lay a foundation for stability control in later period.

3 Elastic–plastic analytical analysis of stress and range of PFZ in surrounding rock

3.1 Analytical solutions of stress

When solving the analytical solutions of the stress and the range of PFZ in surrounding rock under high geostress, we make some assumptions as follows:

(1) Simplify the traditional "three-zones (fracture zone, plastic zone and elastic zone)" failure model of the surrounding rock formed by stress redistribution caused after roadway excavation into the "two-zones (PFZ and elastic zone)" failure model, as shown in Figure 3. This is mainly because, both the fracture and plastic zone in roadway are unstable zones that required key prevention and reinforcement support.

(2) Considering that the PFZ in the surrounding rock is only related to the limit equilibrium condition and not to the primary rock stress [13], thus, it is assumed that the stress distribution in the PFZ after roadway excavation still satisfies the axisymmetric static equilibrium equation, that is [30,31]:

$$\frac{d\sigma_r}{dr} + \frac{\sigma_r - \sigma_\theta}{r} = 0 \tag{1}$$
$$\tau_{r\theta} = 0$$

where σ_r, σ_θ, and $\tau_{r\theta}$ refer to the radial stress, circumferential stress, and tangential stress in roadway surrounding rock, respectively (unit: Pa), r is the polar radius, i.e., the distance from researching point to the roadway center (unit: m), and θ is the polar angle, i.e., the angle of researching point deviating from the polar axis (unit: °).

(3) The surrounding rock in PFZ of roadway satisfies the yield limit equilibrium conditions of the Mohr–Coulomb criterion [30],

$$\sigma_\theta = N\sigma_r + S \tag{2}$$

where $N = (1 + \sin\varphi)/(1 - \sin\varphi)$, $S = (2C\cos\varphi)/(1 - \sin\varphi)$, C is the rock cohesive (unit: Pa), and φ is the internal friction angle of rock (unit: °).

(4) The stress calculation of the roadway is simplified as a plane–strain problem, because the length of the roadway in the axial direction is much larger than the cross-sectional size of the roadway.

3.1.1 Analytical solutions of stress calculation in the PFZ

Based on the above assumptions, substituting equation (2) into equation (1) we obtain:

$$[(N-1)\sigma_r^p + S]^{\frac{1}{N-1}} = re^D \tag{3}$$

where p represents the PFZ of the surrounding rock, σ_r^p is the radial stress in the PFZ, and D is the integral
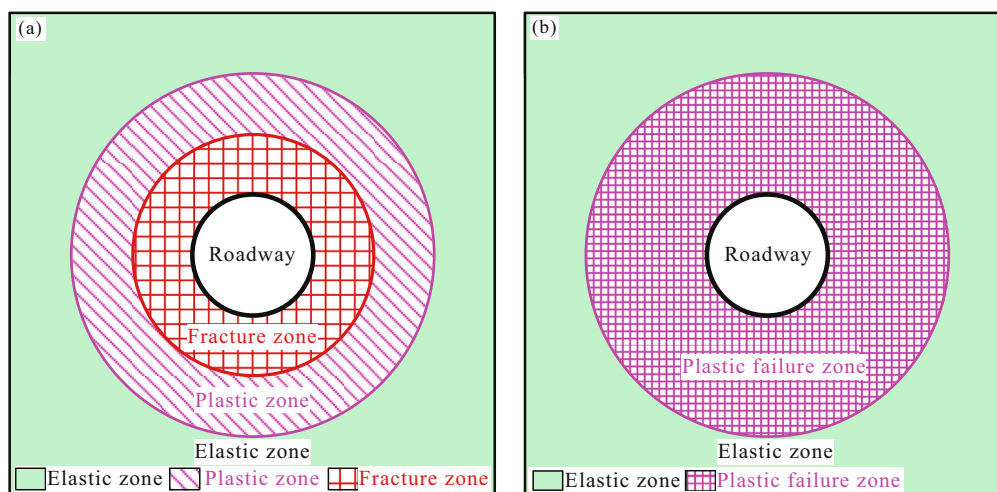
Figure 3: Failure zoning model of the roadway after stress redistribution. (a) "Three-zones" failure model. (b) "Two-zones" failure model.

constant, which can be determined by the boundary conditions. When $r = R_0$ (i.e., the researching point located on the surface of roadway, R_0 is the radius of roadway, and the unit is m), the radial stress $\sigma_r^p = 0$. In this case, we obtain:

$$e^D = \frac{1}{R_0} S^{\frac{1}{N-1}} \tag{4}$$

Equation (4) can be substituted into equation (3) to obtain the radial stress in the PFZ:

$$\sigma_r^p = \frac{S}{N-1}\left[\left(\frac{r}{R_0}\right)^{N-1} - 1\right] \quad (r \leqslant R_p) \tag{5}$$

R_p is the range of PFZ of the surrounding rock (unit: m, and its value is to be determined later).

Equation (5) can be substituted into equation (2) to obtain the circumferential stress in the PFZ (equation (6)):

$$\sigma_\theta^p = \frac{S}{N-1}\left[N\left(\frac{r}{R_0}\right)^{N-1} - 1\right] \quad (r \leqslant R_p) \tag{6}$$

3.1.2 Analytical solutions of stress in elastic zone

The PFZ will be formed in the shallow surrounding rock of roadway during the stress redistribution after the roadway excavation, while the surrounding rock outside the PFZ is still in elastic status. As the stress solutions in the PFZ have been obtained, the surrounding rock outside the PFZ of roadway is simplified to a uniform compression and bilateral compression mechanical model, as shown in Figure 4b and c, so as to obtain the analytical solutions of stress in the elastic zone of roadway.

For the uniform compressed roadway shown in Figure 4b, the radial stress, circumferential stress, and tangential stress can be obtained by using Lame's solutions of ring or cylinder subjected to uniform pressure in elasto mechanics [30–34], respectively:

$$(\sigma_r^e)_b = \frac{R_p^2}{r^2}\sigma_{R_p}^p + \left(1 - \frac{R_p^2}{r^2}\right)\sigma_V \quad (r \geqslant R_p) \tag{7a}$$

$$(\sigma_\theta^e)_b = -\frac{R_p^2}{r^2}\sigma_{R_p}^p + \left(1 + \frac{R_p^2}{r^2}\right)\sigma_V \quad (r \geqslant R_p) \tag{7b}$$

$$(\tau_{r\theta}^e)_b = 0 \quad (r \geqslant R_p) \tag{7c}$$

where e represents the elastic zone of the surrounding rock, $\sigma_{R_p}^p$ is the radial stress at the interface between the elastic zone and the PFZ of the surrounding rock (unit: Pa, and its value is to be determined later), $\sigma_V = \rho g h$ is the average weight of the overlying strata on the roadway (unit: Pa), ρ is the average density of overlying strata (unit: kg/m³), g is the gravitational acceleration (unit: m/s²), and h is the buried depth of roadway (unit: m).

For the bilateral compressed roadway shown in Figure 4c, the radial stress, circumferential stress, and tangential stress can be obtained by using Chilsey's solution of the plate with circular holes' loaded uniform pressure on the opposite sides in elasto mechanics [32,34], respectively:

$$(\sigma_r^e)_c = \frac{\lambda - 1}{2}\left(1 - \frac{R_p^2}{r^2}\right)\sigma_V + \frac{\lambda - 1}{2}\left(1 - \frac{R_p^2}{r^2}\right)$$
$$\left(1 - 3\frac{R_p^2}{r^2}\right)\sigma_V \cos2\theta \quad (r \geqslant R_p) \tag{8a}$$
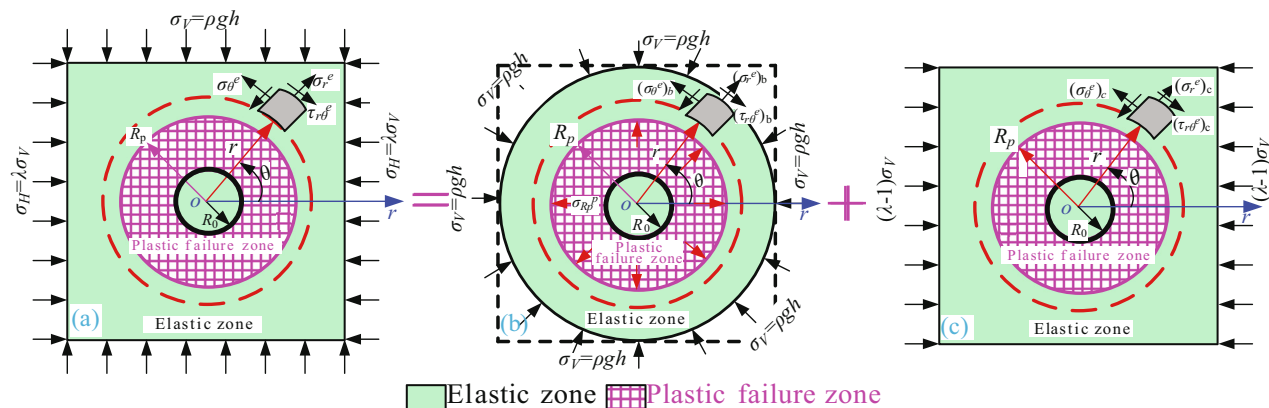
Figure 4: Elastoplastic mechanical model of the roadway: (a) non-uniform compressed roadway; (b) uniform compressed roadway; (c) bilateral compressed roadway.

$$(\sigma_\theta^e)_c = \frac{\lambda - 1}{2}\left(1 + \frac{R_p^2}{r^2}\right)\sigma_V$$

$$- \frac{\lambda - 1}{2}\left(1 + 3\frac{R_p^4}{r^4}\right)\sigma_V \cos2\,\theta \quad (r \geqslant R_p) \tag{8b}$$

$$(\tau_{r\theta}^e)_c = (\tau_{r\theta}^e)_c = -\frac{\lambda - 1}{2}\left(1 - \frac{R_p^2}{r^2}\right)$$

$$\left(1 + 3\frac{R_p^2}{r^2}\right)\sigma_V \sin2\,\theta \quad (r \geqslant R_p) \tag{8c}$$

where λ is the lateral pressure coefficient and a dimensionless quantity, which is the stress ratio between horizontal and vertical.

The stress field in elastic zone of the roadway (Figure 4a) can be obtained by superposing the stress field from equations (7) and (8), that is [14,31,34,35]:

$$\sigma_r^e = (\sigma_r^e)_b + (\sigma_r^e)_c = \frac{R_p^2}{r^2}\sigma_{R_p}^p + \frac{\lambda + 1}{2}\left(1 - \frac{R_p^2}{r^2}\right)\sigma_V$$

$$+ \frac{\lambda - 1}{2}\left(1 - \frac{R_p^2}{r^2}\right)\left(1 - 3\frac{R_p^2}{r^2}\right)\sigma_V \cos2\,\theta \quad (r \geqslant R_p) \tag{9a}$$

$$\sigma_\theta^e = (\sigma_\theta^e)_b + (\sigma_\theta^e)_c = -\frac{R_p^2}{r^2}\sigma_{R_p}^p + \frac{\lambda + 1}{2}\left(1 + \frac{R_p^2}{r^2}\right)\sigma_V$$

$$- \frac{\lambda - 1}{2}\left(1 + 3\frac{R_p^4}{r^4}\right)\sigma_V \cos2\,\theta \quad (r \geqslant R_p) \tag{9b}$$

$$\tau_{r\theta}^e = (\tau_{r\theta}^e)_b + (\tau_{r\theta}^e)_c = -\frac{\lambda - 1}{2}\left(1 - \frac{R_p^2}{r^2}\right)$$

$$\left(1 + 3\frac{R_p^2}{r^2}\right)\sigma_V \sin2\,\theta \quad (r \geqslant R_p) \tag{9c}$$

3.2 Analytical solution of the range of PFZ

According to the continuity of stress at the interface between the elastic zone and the PFZ, there are $\sigma_r^e = \sigma_r^p$, $\sigma_\theta^e = \tau_\theta^p$, and $\tau_{r\theta}^e = \tau_{r\theta}^p$ when $r = R_p$. Thus, we obtain:

$$\left(\frac{R_p}{R_0}\right)^{N-1}$$

$$= \frac{((\lambda + 1)\sigma_V - 2(\lambda - 1)\sigma_V \cos2\,\theta)(N - 1) + 2S}{(N + 1)S} \tag{10}$$

This equation (10) is the calculation formula for determining the range of PFZ of the roadway. Based on the continuity condition of stress $\sigma_r^e = \sigma_r^p$ at the interface, substituting it into equation (10) we obtain the radial stress $\sigma_{R_p}^p$ as follows:

$$\sigma_{R_p}^p = \frac{((\lambda + 1)\sigma_V - 2(\lambda - 1)\sigma_V \cos2\,\theta) - S}{N + 1} \tag{11}$$

The stress field in the elastic zone of the roadway is determined by substituting equation (11) into equation (9).

4 Characteristics of stress and PFZ in the roadway surrounding rock

Due to the difficulty in obtaining the analytical solutions of the stress and range of PFZ in roadway under the non-uniformly horizontal geostress, they were numerically studied by using the general finite difference software FLAC^{3D}. Figure 5 shows the three-dimensional numerical model of the actually excavated circular roadway with the radius of 2.5 m. In this model dimensions are 50 × 50 × 50 m. The top of the model is subjected to a uniform
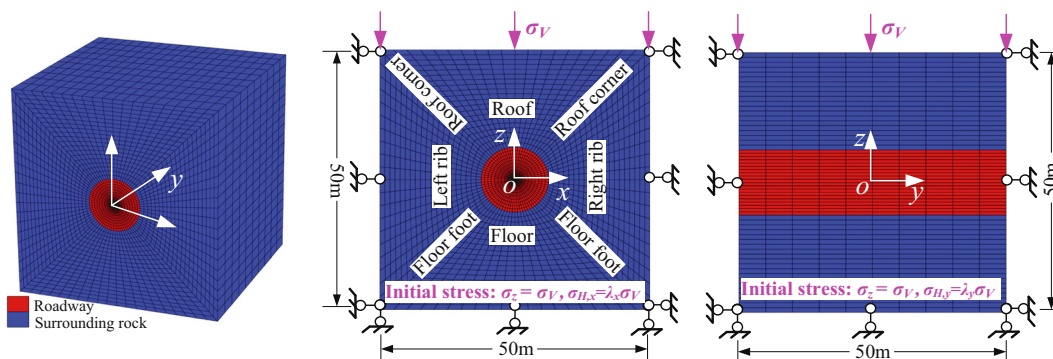

Figure 5: Three-dimensional numerical analysis model of the roadway.

vertical stress σ_V of 20.00 MPa, and the whole model has initial stress in three directions of x, y, z, which are $\sigma_{H,x} = \lambda_x \sigma_V$, $\sigma_{H,y} = \lambda_y \sigma_V$, σ_V, respectively, where λ_x and λ_y are lateral pressure coefficients in the horizontal x-direction and y-direction, respectively. The normal displacement constraint is set around and at the bottom of the numerical model (Figure 5). Through drilling exploration and related tests, the lithology and physical and mechanical properties of roadway surrounding rocks in the fault tectonic area have been obtained, as shown in Table 2. Since the roadway is arranged in the mudstone layer, and the influence range of the roadway excavation is smaller than the thickness of the mudstone layer, the physical and mechanical parameters of the surrounding rock used are shown in Table 3 during the numerical calculation.
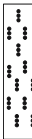
When studying the influence of the uniformly horizontal geostress (i.e., horizontal stresses are evenly distributed but different than vertical and can be equal in each horizontal direction) on the stress and the PFZ of surrounding rock, the lateral pressure coefficients $\lambda_x = \lambda_y = 0.5, 1.0, 1.5,$ and 2.0 were taken during the numerical simulation. When discussing the influence of the non-uniformly horizontal geostress on the stress and the PFZ, the lateral pressure coefficients $\lambda_y = 0.5, \lambda_x = 0.5, 1.0, 1.5, 2.0; \lambda_y = 1.0, \lambda_x = 1.0, 1.5, 2.0; \lambda_y = 1.5, \lambda_x = 1.5, 2.0; \lambda_y = 2.0,$ and $\lambda_x = 2.0$ were taken, considering the rotation symmetry of horizontal stress. In the actual simulation, we first simulate the initial stress balance of the surrounding rock and then simulate the stress balance and failure characteristics after excavating.

4.1 Characteristics of stress and PFZ under the uniformly horizontal geostress

4.1.1 Distribution characteristics of stress in the surrounding rock

The comparison results between the analytical and numerical solutions of stress in the surrounding rock given in Figure 6 show that their change trend and law are basically the same. Moreover, except that the circumferential stress in the roadway right rib has a maximum difference of 15% when the lateral compression coefficient is 2 (Figure 6b), their stress values are also consistent. This shows that in the three-dimensional numerical simulation of the stress of roadway surrounding rock, the numerical simulation method of taking the non-uniform ground stress as the initial stress

Table 2: Lithology and physical and mechanical properties of roadway surrounding rocks

Rock style	Synthesis column map	Rock stratum thickness (m)	Buried depth h (m)	Bulk modulus K (GPs)	Shear modulus G (GPs)	Cohesive force C (Mpa)	Internal fraction angle φ (°)	Tensile strength σ_t (MPa)	Density ρ (kg/m³)
Siltstone		9.85–15.87 (12.36)	−778.11	5.94	4.05	1.83	32	1.16	2,600
Fine sandstone		6.78–10.23 (8.85)	−790.47	7.62	5.24	2.45	35	1.23	2,700
Mudstone		13.75–18.26 (16.51)	−799.32	1.56	0.94	1.75	28	0.80	2,500
Sandy mudstone		2.83–3.16 (2.99)	−815.83	1.52	0.89	1.69	26	0.83	2,480
Mudstone		14.63–23.25 (18.45)	−818.82	1.56	0.94	1.75	28	0.80	2,500
Aluminum mudstone		1.42–2.19 (1.71)	−837.27	1.49	0.84	1.56	25	0.78	2,400
Mudstone		19.26–26.38 (23.58)	−838.98	1.56	0.94	1.75	28	0.80	2,500
Siltstone		9.27–14.35 (11.81)	−862.56	5.94	4.05	1.83	32	1.16	2,600
Fine sandstone		3.27–5.63 (4.45)	−874.37	7.62	5.24	2.45	35	1.23	2,700

Table 3: Physical and mechanical parameters of the surrounding rock

Density ρ (kg/m^3)	Buried depth h (m)	Bulk modulus K (GPa)	Shear modulus G (GPa)	Cohesive force C (MPa)	Internal friction angle φ (°)	Tensile strength σ_t (MPa)
2,500	800	1.56	0.94	1.75	28.0	0.80

is correct and feasible, and the assumptions and methods used in the analytical calculation of stress in excavated roadway are reasonable. This provides a simplified analytical calculation method for analyzing the stress field and plastic failure of the roadway after excavation disturbance.

As can seen from Figure 6, the stress-released area, stress-concentration area, and primary rock stress area of circumferential stress in roadway are obviously distinguished during the process of stress redistribution after the excavation and other disturbances. However, the distribution range and characteristics of each area are significantly different. The range of the circumferential stress-released area in the roadway roof increases gradually with the growth of lateral pressure coefficient λ_x, which sharply increased from 0.56 m at $\lambda_x = 0.5$ to 3.39 m at $\lambda_x = 2.0$, an increase of about 505% (Figure 6a and Table 4). While the range of circumferential stress-released area in the roadway roof corner and floor foot is slower, increasing by about 117% (see Figure 6c and Table 4). However, the range of the circumferential stress-released area in the roadway ribs reduced slowly with the growth of lateral pressure coefficient λ_x, and its value decreased from 1.93 m at $\lambda_x = 0.5$ to 1.75 m at $\lambda_x = 2.0$, a decrease of about 9% (Figure 6b and Table 4). Considering the destruction of original stress equilibrium state in the stress-released area, the surrounding rock is more prone to be deformed and fractured.

In the circumferential stress-concentration area of roadway ribs, with the increase of the lateral pressure coefficient λ_x, the maximum circumferential stress decreases from 38.20 MPa at $\lambda_x = 0.5$ to 25.72 MPa at $\lambda_x = 2.0$, with a decline of about 33%, and the corresponding stress-concentration factor K (K = maximum stress/initial (*in situ*) rock stress) decreases from 1.87 to 1.22 (Table 4), which shows a feature of decrease (Figure 6b). However, the circumferential stress in the stress-concentration area of roadway roof increases with the increase of the lateral pressure coefficient λ_x (Figure 6a and c), and its value increases from 10.35 MPa at $\lambda_x = 0.5$ to 42.60 MPa at $\lambda_x = 2.0$, an increase of about 317%, and the corresponding stress-concentration factor K also increases from 1.28 to 1.76 (Table 4). This further indicates that the stress distribution in the surrounding

rock is strongly affected by the deep high geostress, and the change of the stress will further affect the deformation and failure of the roadway. That is to say, the deep high geostress makes roadway roof and roadway floor more easily destroyed than roadway ribs. Therefore, it is necessary to pay special attention to the control of the roadway roof, roof corner, and floor foot when strengthening and supporting the roadway under deep high geostress.

It can be seen from the combination of Figure 6b–d that, unlike the circumferential stress, the radial stress in the roadway does not form the obvious stress-concentration area during the stress redistribution process after the excavation and other disturbances, and the maximum radial stress is basically equal to the primary rock stress. These factors indicate that the main control stress affecting roadway deformation and failure is the circumferential stress under the action of deep high geostress.

4.1.2 Distribution characteristic of the PFZ

Figure 7 shows that the overall change law and distribution characteristics of the numerical and analytical solutions of the range of PFZ in surrounding rocks are the same. Combined with Table 5, except that the relative errors ((numerical solution–analytical solution)/ analytical solution × 100%) of the range of PFZ in the roadway ribs and the roof corner (i.e., $\theta \leq 45°$) exceed 15% when the lateral pressure coefficient $\lambda_x = 2.0$, the relative errors in other surrounding rocks are within 10%. As a result, it is further proved that the analytical calculation and numerical simulation method for the range of PFZ and the stress field in this paper are reasonable and reliable.

According to Figure 7 and Table 5, the range of PFZ in the roadway ribs gradually decreases with the increase of lateral pressure coefficient λ_x, and its value has decreased from 3.40 m at $\lambda_x = 0.5$ to 1.35 m at $\lambda_x = 2.0$, with a reduction of about 1.5 times. On the contrary, the range of PFZ in the roadway roof and floor increases sharply with the growth of λ_x, its value has increased from 0.45 m at $\lambda_x = 0.5$ to 5.93 m at $\lambda_x = 2.0$, with an increase of about 12 times. Furthermore, the distribution
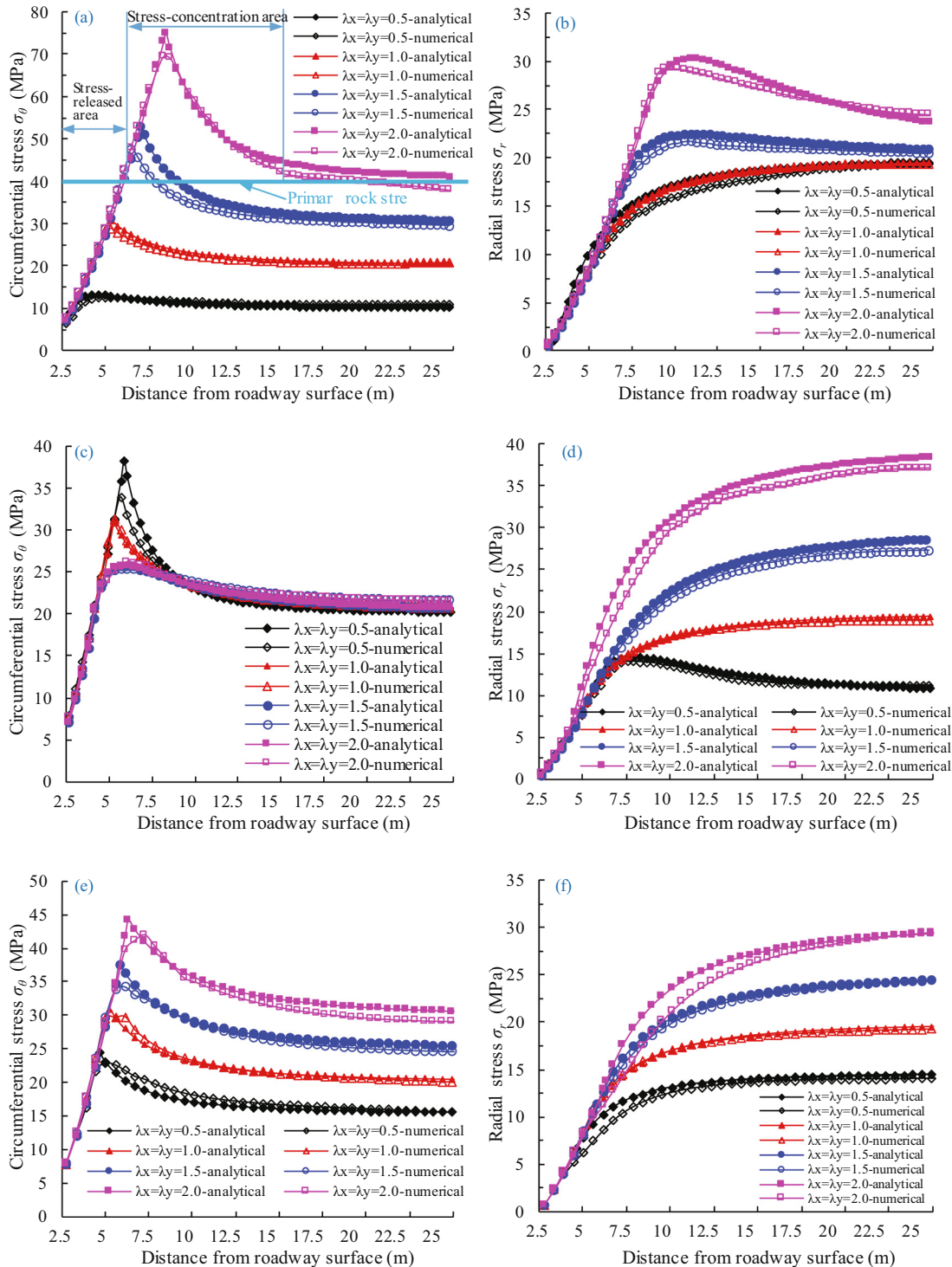
Figure 6: Contrast curves of circumferential and radial stresses in roadway surrounding rocks under different lateral pressure coefficients: (a) and (b) roadway roof; (c) and (d) right rib of the roadway; (e) and (f) roadway roof corner.

of the PFZ is diversified under different lateral pressure coefficients λ_x. When the $\lambda_x < 1.0$ (i.e., under the condition of non-uniform pressure and vertical stress

as the maximum stress), the PFZ in the surrounding rock is of a horizontal gourd shape. When the coefficient $\lambda_x = 1.0$ (i.e., under the condition of non-uniform pressure),

Table 4: The value, range, and concentration factor of stress under different lateral pressure coefficients

Stress		Circumferential stress σ_θ (MPa)				Radial stress σ_r (MPa)			
Lateral pressure coefficients		$\lambda = 0.5$	$\lambda = 1.0$	$\lambda = 1.5$	$\lambda = 2.0$	$\lambda = 0.5$	$\lambda = 1.0$	$\lambda = 1.5$	$\lambda = 2.0$
Roof	Stress-released area (m)	0.56	1.88	2.81	3.39	15.94	15.94	6.19	6.19
	Stress-concentration area (m)	12.50	10.80	10.25	9.30	0	0	6.88	6.88
	Stress-concentration factor K	1.28	1.48	1.68	1.76	0	0	1.04	1.17
	Primary rock stress (MPa)	10.35	20.91	31.53	42.60	19.13	19.08	21.39	25.89
Right rib	Stress-released area (m)	1.93	2.01	1.65	1.75	3.39	15.94	15.46	15.94
	Stress-concentration area (m)	11.14	10.68	11.69	11.32	10.03	0	0	0
	Stress-concentration factor K	1.87	1.48	1.22	1.22	1.27	0	0	0
	Primary rock stress (MPa)	20.52	20.91	21.12	21.09	11.55	19.09	27.60	37.14
Roof corner	Stress-released area (m)	1.26	1.79	2.28	2.74	22.93	22.93	24.40	25.43
	Stress-concentration area (m)	19.17	18.68	18.15	17.18	0	0	0	0
	Stress-concentration factor K	1.57	1.51	1.47	1.45	0	0	0	0
	Primary rock stress (MPa)	15.55	20.48	25.47	30.51	14.49	19.52	24.48	29.36

Note: stress concentration factor K = maximum stress/initial (*in situ*) rock stress.
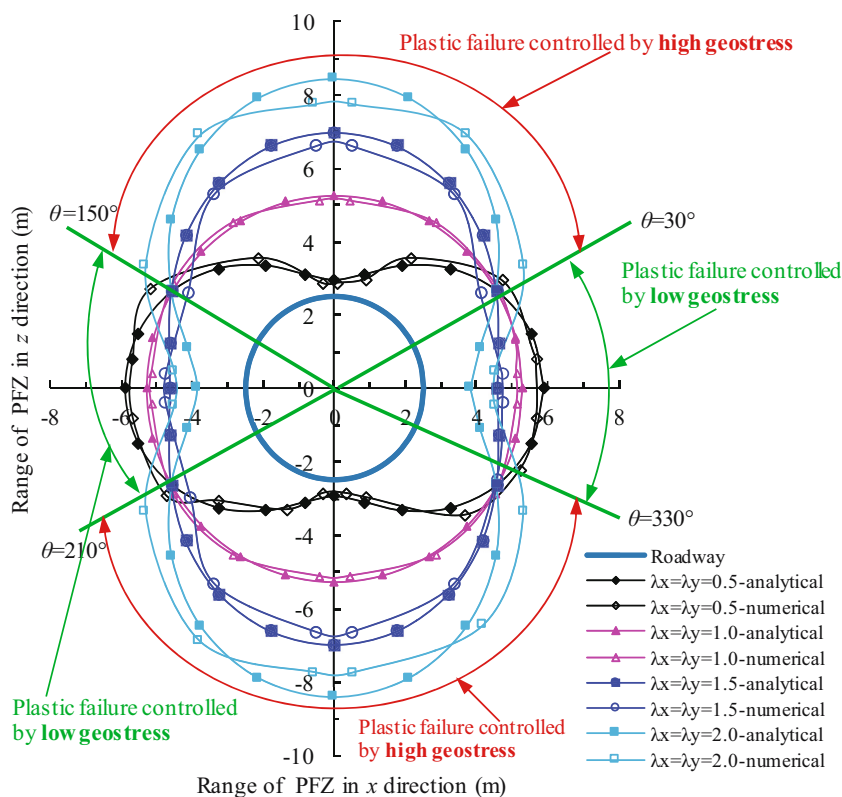
Figure 7: Distribution characteristics of the PFZ in roadway surrounding rock.

the PFZ in the surrounding rock is an approximately circular distribution. When the coefficient $\lambda_x > 1.0$ (i.e., under the condition of non-axisymmetric pressure and horizontal stress as the maximum stress), the PFZ in the surrounding rock changes into a vertical gourd shape.

Thus, it shows that the roof and floor of roadway are more easily deformed and fractured than the ribs of roadway under the high geostress. In other words, the roadway roof and floor are more easily and strongly affected by deep high geostress. This is also consistent

Table 5: Comparison of the range of PFZ in surrounding rocks at different angles θ

Lateral pressure coefficient λ	$(R_p - R_0)/R_0$	Angle θ (°)						
		0	15	30	45	60	75	90
0.5	Analytical solutions	2.36	2.29	2.11	1.84	1.54	1.28	1.18
	Numerical solutions	2.29	2.17	2.34	2.07	1.66	1.24	1.15
	Relative error (%)	−2.97	−5.24	10.90	12.50	7.79	−3.13	−2.54
1.0	Analytical solutions	2.11	2.11	2.11	2.11	2.11	2.11	2.11
	Numerical solutions	1.98	2.05	2.03	1.96	2.04	2.01	1.98
	Relative error (%)	−6.16	−2.84	−3.79	−7.11	−3.32	−4.74	−6.16
1.5	Analytical solutions	1.84	1.92	2.11	2.36	2.58	2.74	2.80
	Numerical solutions	1.82	1.89	1.85	2.24	2.41	2.48	2.68
	Relative error (%)	−1.10	−1.59	-12.32	−5.08	−6.59	−9.49	−4.29
2.0	Analytical solutions	1.54	1.71	2.11	2.58	2.99	3.27	3.37
	Numerical solutions	1.81	2.08	2.51	3.14	3.05	2.94	3.14
	Relative error (%)	17.53	21.64	18.96	21.71	2.01	−10.09	−6.82

with the distribution law of circumferential stress in surrounding rock with lateral pressure coefficient obtained previously. Therefore, when reinforcing the roadway with deep high geostress, some stronger supporting measures should be focused on the roof and floor of the roadway, so as to control the deformation and failure of the roadway.

Furthermore, it can also be seen from Figure 7 that the range of PFZ shows an increasing trend as the lateral pressure coefficient λ_x increases in the roadway surrounding rock region where the polar angle θ is greater than 30° and less than 150° ($30° \leq \theta \leq 150°$), and is greater than 210° and less than 330° ($210° \leq \theta \leq 330°$). The biggest change occurs in the roadway roof and floor, that is, the plastic failure of surrounding rock in this area is controlled by high geostress. However, the range of PFZ in the surrounding rock outside this region (i.e., $−30° \leq \theta \leq 30°$ and $150° \leq \theta \leq 210°$) decreases with the increase of the lateral pressure coefficient λ_x. And the change is greatest in the roadway ribs, that is, the plastic failure of surrounding rock in this area is controlled by low geostress.

## 4.2 Characteristics of the stress and PFZ under the non-uniformly horizontal geostress

4.2.1 Distribution characteristics of the stress in surrounding rock

According to the comprehensive analysis of Figure 8 and Table 6, the maximum principal stress in the roadway roof and floor will gradually increase with the growth of λ_x if the horizontal lateral pressure coefficient λ_y remains unchanged under the non-uniformly horizontal geostress (i.e., horizontal lateral pressure coefficient $\lambda_x \neq \lambda_y$), while the maximum principal stress in the roadway ribs decreases gradually. That is to say, the degree of stress concentration in the roof and floor increases gradually, while the degree of stress concentration in ribs decreases gradually (Figure 8a–c or Figure 8d–f or Figure 8g and h). Besides, the smaller λ_y is, the greater the value of maximum principal stress and the degree of stress concentration in roadway roof and floor will be. When $\lambda_y = 0.5$, the maximum principal stress increases from 19.37 MPa at $\lambda_x = 0.5$ to 47.13 MPa at $\lambda_x = 1.5$, with an increase of about 1.43 times (Table 6). However, as the λ_y increases, the maximum principal stress and degree of stress concentration in the roadway surrounding rock change only slightly if the λ_x remains unchanged (Figure 8b–d or Figure 8c, e–g and Table 6).

According to the above analysis, we can speculate that the main control stress of affecting roadway deformation and failure is horizontal stress in the x-direction (i.e., perpendicular to the roadway strike). It causes the relatively larger stress and stress-concentration area to appear in the roadway roof and floor, and to promote this area in becoming the main deformation and failure area. As a result, when designing the roadway strike, it is necessary to try to avoid it become perpendicular to the direction of the maximum horizontal stress, so as to reduce the roadway deformation and failure.
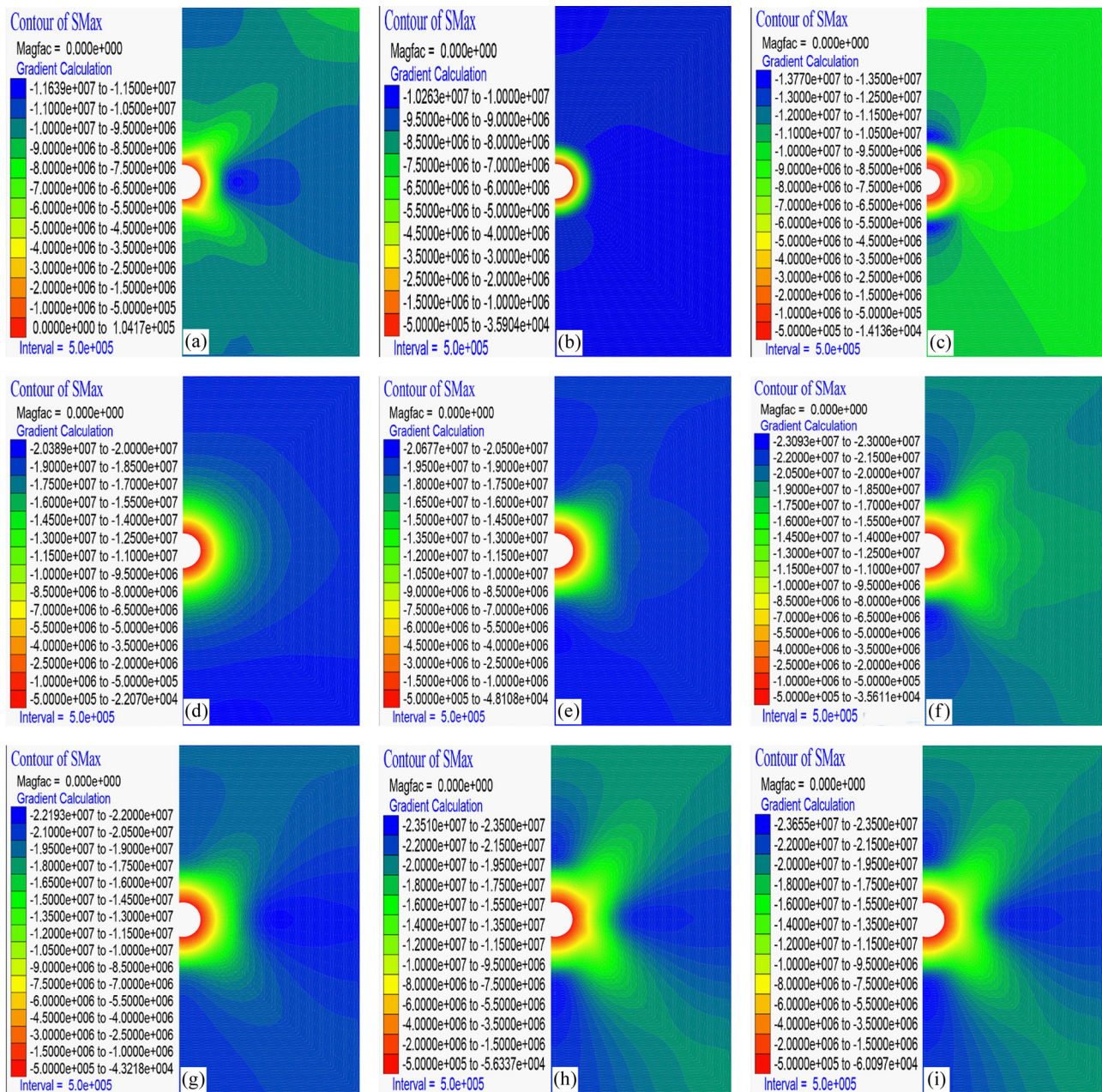
Figure 8: Distribution of the maximum principal stress under different lateral pressure coefficients. (a) $\lambda_x = 0.5$, $\lambda_y = 0.5$; (b) $\lambda_x = 1.0$, $\lambda_y = 0.5$; (c) $\lambda_x = 1.5$, $\lambda_y = 0.5$; (d) $\lambda_x = 1.0$, $\lambda_y = 1.0$; (e) $\lambda_x = 1.5$, $\lambda_y = 1.0$; (f) $\lambda_x = 2.0$, $\lambda_y = 1.0$; (g) $\lambda_x = 1.5$, $\lambda_y = 1.5$; (h) $\lambda_x = 2.0$, $\lambda_y = 1.5$; (i) $\lambda_x = 2.0$, $\lambda_y = 2.0$

## 4.2.2 Distribution characteristic of the PFZ

When the horizontal lateral pressure coefficients λ_x and λ_y have different combinations, the PFZ in the roadway surrounding rocks under the non-uniformly horizontal geostress (i.e., horizontal lateral pressure coefficient $\lambda_x \neq \lambda_y$) will present different shapes, such as elliptical shapes, vertical gourd shapes, and butterfly shapes and so on. However, under the same λ_y, the shape of PFZ is mainly controlled by the λ_x. When $\lambda_y = 0.5$, the shape of PFZ

changes from horizontal gourd shape (Figure 9a) to circular shape (Figure 9d) and then to an approximate butterfly shape (Figure 9g) with the increase of λ_x. This portends the above analysis on the shape of PFZ that with the increase of the λ_x, the PFZ in surrounding rocks gradually transfers from the roadway ribs to the roadway roof and floor.

The specific range of PFZ and regularity of PFZ can be obtained from Figure 9j: under the same conditions of λ_y, the range of PFZ in the roadway roof and floor shows

Table 6: The maximum and minimum values of the maximum principal stress under different lateral pressure coefficients

Surrounding rock region	Stress (MPa)	Lateral pressure coefficient								
		$\lambda_y = 0.5$			$\lambda_y = 1.0$			$\lambda_y = 1.5$		$\lambda_y = 2.0$
		$\lambda_x = 0.5$	$\lambda_x = 1.0$	$\lambda_x = 1.5$	$\lambda_x = 1.0$	$\lambda_x = 1.5$	$\lambda_x = 2.0$	$\lambda_x = 1.5$	$\lambda_x = 2.0$	$\lambda_x = 2.0$
Roof	$\sigma_{1,max}$	19.37	28.83	47.13	28.86	47.53	61.87	47.63	61.60	61.96
	$\sigma_{1,min}$	6.57	7.62	7.72	7.53	7.77	7.74	7.81	7.76	7.74
Right rib	$\sigma_{1,max}$	33.95	31.37	25.44	31.39	26.38	32.91	29.50	32.84	38.83
	$\sigma_{1,min}$	7.84	7.75	7.61	7.63	7.71	7.72	7.70	7.69	7.61
Roof corner	$\sigma_{1,max}$	23.49	29.89	33.50	29.75	34.00	40.61	33.94	40.61	40.51
	$\sigma_{1,min}$	7.94	7.95	8.01	7.86	8.00	7.95	7.99	7.99	7.97
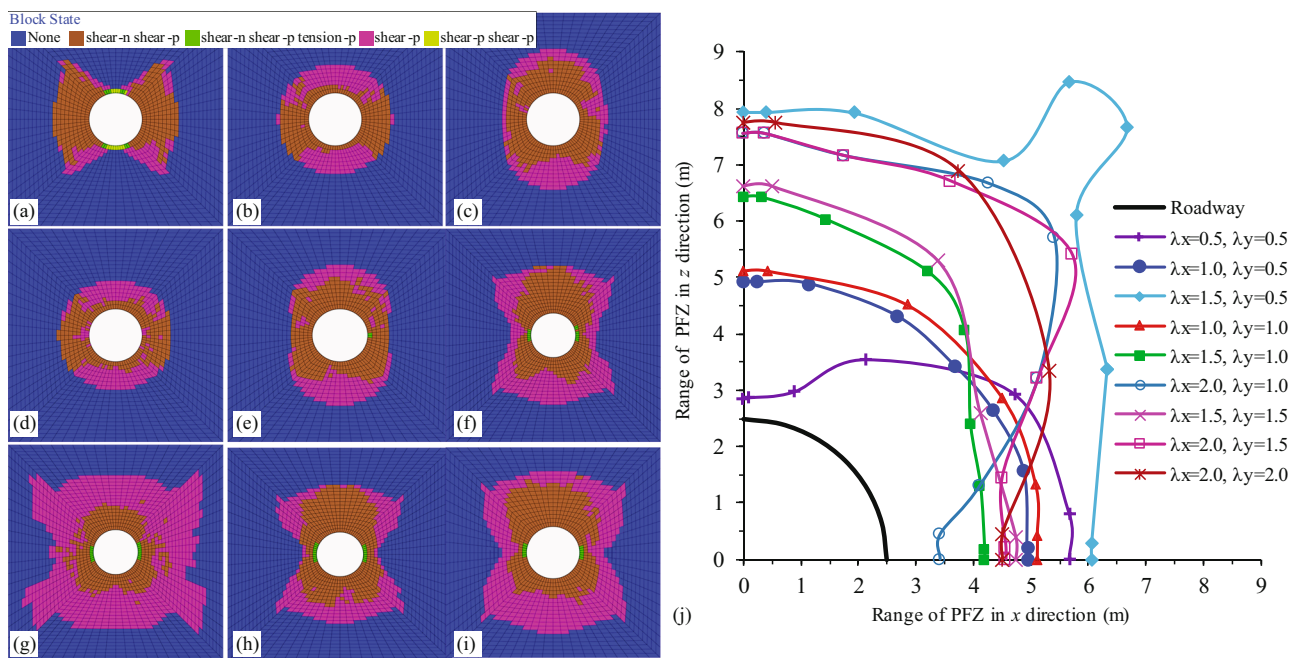
Figure 9: The shape and range of PFZ in the roadway surrounding rock under the non-uniformly horizontal geostress. (a) $\lambda_x = 0.5$, $\lambda_y = 0.5$, (b) $\lambda_x = 1.0$, $\lambda_y = 1.0$, (c) $\lambda_x = 1.5$, $\lambda_y = 1.5$, (d) $\lambda_x = 1.0$, $\lambda_y = 0.5$, (e) $\lambda_x = 1.5$, $\lambda_y = 1.0$, (f) $\lambda_x = 2.0$, $\lambda_y = 1.5$, (g) $\lambda_x = 1.5$, $\lambda_y = 0.5$, (h) $\lambda_x = 2.0$, $\lambda_y = 1.0$, (i) $\lambda_x = 2.0$, $\lambda_y = 2.0$, (j) range of PFZ in surrounding rock.

a growth trend with the increase of the λ_x. Moreover, the smaller λ_y is (i.e., greater value of λ_x/λ_y), the more obvious the increase in the range of PFZ will be. For example, when $\lambda_y = 0.5$, with the increase of λ_x from 0.5 to 1.5, the range of PFZ in the roadway roof and floor increases from 0.45 to 5.44 m, with an increase of about 12 times. While the range of PFZ in the roadway ribs decreases slowly as a whole (Figure 9b–h), and the decreasing trend is less obvious with the increase of λ_y. When the ratio of horizontal lateral pressure coefficients λ_x and λ_y (i.e., λ_x/λ_y) is too large, a large PFZ will occur in the roadway roof, floor, and ribs (Figure 9g), and even the entire surrounding rock will be completely destroyed, which

may further lead to the failure of normal operation of numerical simulation (when $\lambda_x/\lambda_y > 3$).

5 Stability control technology of the roadway in deep fault tectonic fracture area

5.1 Supporting scheme

Based on the engineering geological conditions and *in situ* stress test results of the No. 105 mining area of the
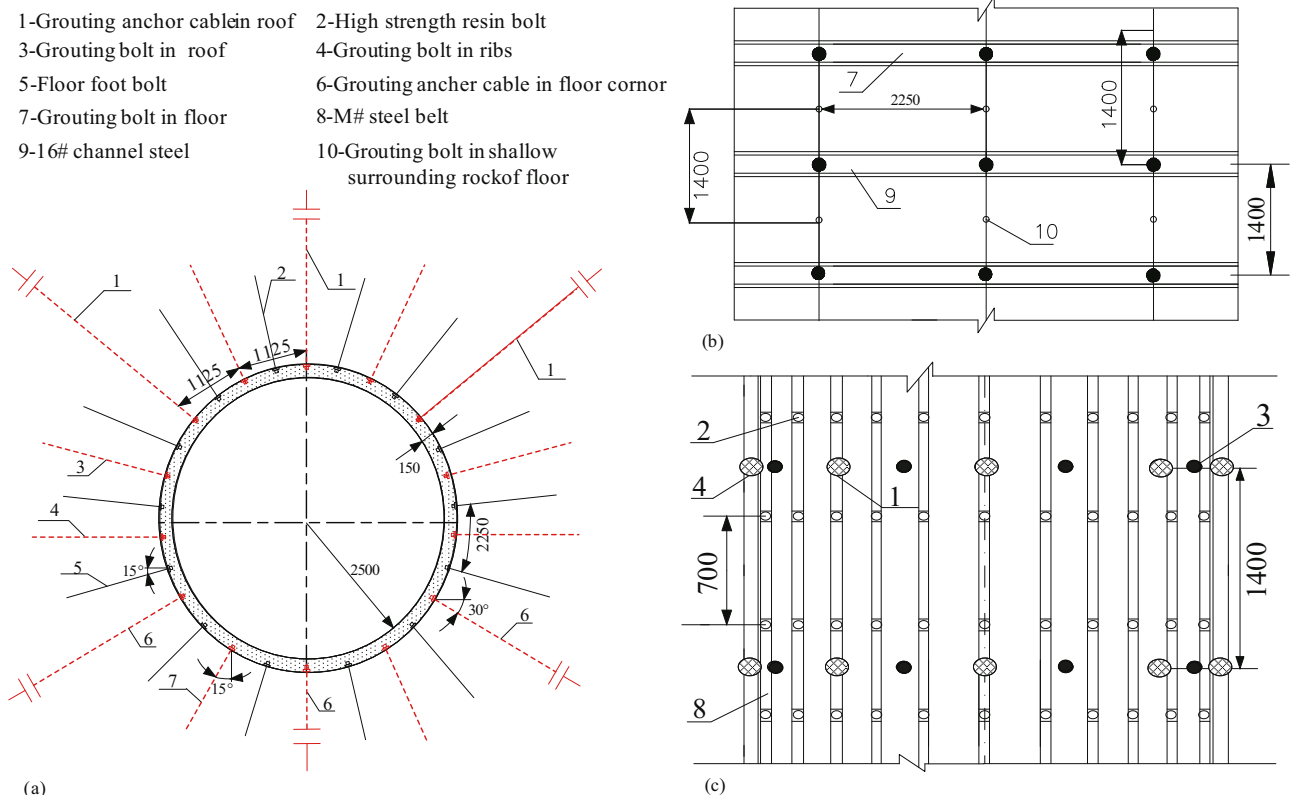
Yuandian Mine in Huaibei, the horizontal stress has strong directional characteristics (i.e., the horizontal lateral pressure coefficients λ_x and λ_y are about 1.35 and 0.65, respectively, and $\lambda_x/\lambda_y = 2.11$). In view of considering the long-term safety of roadway support, the distribution characteristics and range of the PFZ in the roadway are obtained from the results of the numerical analysis at $\lambda_x = 1.5$ and $\lambda_y = 0.5$ given in part 4.2.2 of this paper as the basic reference for the roadway support design. It is known from Figure 9g and j that, under the high and non-uniform geostress, that is, $\lambda_x = 1.5$ and $\lambda_y = 0.5$, the damage of the roadway roof corner is the most serious, followed by the roadway roof and floor, and the roadway ribs are the smallest, and its range of PFZ is about 7.96, 5.44, and 3.56 m, respectively. The PFZ is of an approximately vertical "gourd" shape.

Aiming at the highly fractured roadway in the deep subsurface faulted area, some engineering practices have demonstrated that the bolt-cable-grouting reinforcement can effectively control the deformation and failure of roadway [19,36–39]. In order to make the shallow broken surrounding rock of roadway form a complete grouting reinforcement circle after grouting, and form local reinforcement consolidation bodies in surrounding rocks far away from the roadway surface, the roof, roof corner, and floor foot of roadway are supported by grouting anchor cables. And the roadway ribs and floor are supported by grouting bolts. In addition, the whole cross-section of the roadway is supported by the bolting and shotcreting with wire mesh to ensure the safety and long-term effectiveness of roadway support. Finally, a combined support scheme focused on "bolting and shotcreting with wire mesh + deep–shallow coupling full-section bolt-cable-grouting" was formed. Figure 10 shows the detailed design of the supporting scheme, and the following are specific supporting parameters of this scheme:

(1) Deep–shallow coupling full-section bolt-cable-grouting: the thread steel hollow bolt (specification: $\Phi25 \times 3,500$ mm, breaking force $\geq$ 15t) shall be selected for grouting bolt. Moreover, 6 mm grouting holes are drilled sequentially on the bolt body, the bolt tail is smashed flat, and the quick-hardening cement cartridge is used to seal the borehole. There

1-Grouting anchor cablein roof   2-High strength resin bolt
3-Grouting bolt in roof   4-Grouting bolt in ribs
5-Floor foot bolt   6-Grouting ancher cable in floor cornor
7-Grouting bolt in floor   8-M# steel belt
9-16# channel steel   10-Grouting bolt in shallow surrounding rockof floor

Figure 10: Deep–shallow coupling full-section bolt-cable-grouting combined support scheme for roadway. (a) Bolt-cable-grouting supporting schemein whole section of roadway, (b) bolt-cable-grouting supporting schemein in roof, (c) bolt-cable-grouting supporting schemein floor.

are four grouting bolts in the roadway roof with a row spacing of 2,100 × 1,400 mm, three grouting bolts in the roadway floor with a row spacing of 1,800 × 1,400 mm, and two grouting bolts in the roadway ribs with a row spacing of 2,250 × 1,400 mm. For the grouting anchor cable, the high-strength grouting anchor cables are composed of nine strips of Φ7 mm high-strength and low relaxation pre-stressing steel wires and one strip of Φ13 mm hollow steel pipe, which are rotated as a whole through the screw machine, the center of anchor cable being the grouting pipe. There are six grouting anchor cables with a diameter of 35 mm in the whole section of the roadway, including two at the roof corner and the floor foot with a length of 8,000 mm, and one at the center of the roof and floor with a length of 5,500 mm. And their row spacing is 2,100 × 1,400 mm. During grouting construction, the grouting pressure is 0–1 MPa and the stabilization time is 3–5 min.

(2) High-strength resin bolt: the bolt and bolt body are special-threaded steel bars for left-handed full-thread high-strength bolts. The bolt specification is Φ22 × 2,600 mm, the spacing between rows is 700 × 700 mm, and the thread of bolt tail is M24. The borehole diameter is 28 mm, the anchorage length is 1,000 mm, and the anchorage force of each bolt shall be not less than 80 kN. Each bolt is anchored with two resin cartridges, and the specification is Z2550.

(3) Shotcreting: the selected sprayed concrete grade is C20, the thickness of initial spraying layer after the formation of roadway is 30–50 mm, the thickness of second spraying shall reach 150 mm as per the design, and the concrete raw material ratio is 1:2:2 (cement:sand:stone).

(4) Grouting material: mixture of 325# ordinary portland cement and ACZ-1 cement additive, with water–cement ratio of 0.7:1–1:1.
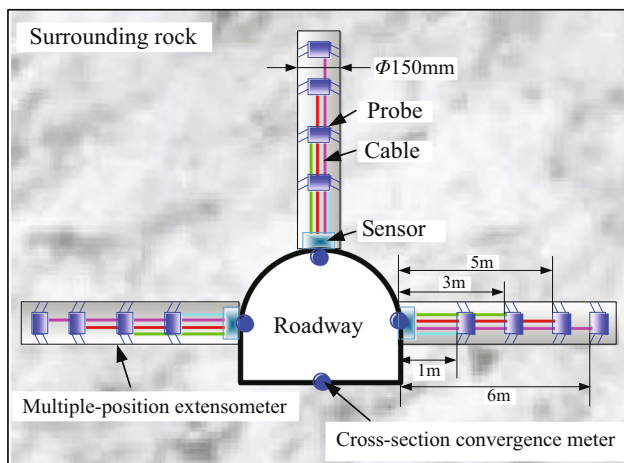

Figure 11: Monitoring point arrangement in roadway surrounding rocks.

5.2 Supporting effect

For the purpose of evaluating the reinforcement effect of this combined support scheme for the roadway in deep broken area, the cross-section convergence meter and the multiple-position extensometer are used for field monitoring of the surface deformation and internal separation deformation of the roadway, respectively. Figure 11 shows the layout of measuring points.

Figure 12 shows the monitored results. The first 50 days of development is the deformation acceleration period of the surrounding rock. The deformation began
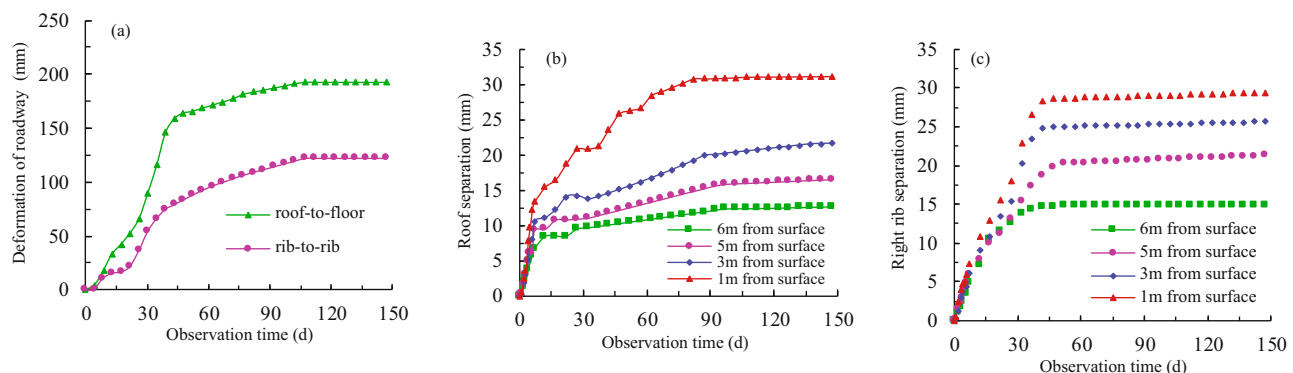
Figure 12: Roadway deformation and separation: (a) roadway deformation; (b) roof separation; and (c) right rib separation.

to slow down between the 50th and the 100th day. The entries were basically stable after the 100th day. The maximum roof-to-floor convergence was 193 mm (Figure 12a), while the maximum rib-to-rib convergence was 123 mm (Figure 12a). These values are within the safe range of the allowable deformation of roadway. It is known from Figure 12b and c that, the closer to the surface of roadway, the larger the deformation of surrounding rock. However, the maximum separation deformation of roadway is less than 30 mm, which is also within the safe range of the allowable deformation of roadway. In additional, the field observations of roadway also suggested that there are only a few places that had large local deformation of the roadway and peeling spray layer due to poor construction and other man-made or environmental factors.

Therefore, it can be proved that the combined support technology of "bolting and shotcreting with wire mesh + deep-shallow coupling full-section bolt-cable-grouting" has effectively controlled the rib spalling, roof subsidence, and floor heave of roadway in deep broken area under the high and non-uniform geostress. This combined support technology achieves the purpose of maintaining the stability of the roadway and saves the supporting economic cost to a certain extent. It also provides a theoretical basis and reference method for the precise support design of roadway in deep broken area under the high and non-uniform geostress.

6 Conclusions

(1) The simplified elastic–plastic mechanical model of the deep buried roadway under the high geostress is constructed, based on the assumption of "two-zones" failure model of roadway. Analytical solutions of the stress and range of PFZ in surrounding rock are deduced by using the Mohr–Coulomb strength criterion. The comparison between analytical solutions and numerical solutions indicates that the relative error of this stress and range of PFZ are less than 15%. It further proves that the analytical and numerical methods used in this paper are correct and reasonable.

(2) Under the uniformly horizontal geostress, as the lateral pressure coefficient increased from 0.5 to 2.0, the circumferential stress, stress-concentration factor, and range of stress-released area in the roadway roof significantly increased by about 4.12 times, 1.38 times, and 6.05 times, respectively. While they decreased in the roadway ribs. The change of radial stress in roadway is much smaller than the change of circumferential stress. That is to say, the deep high geostress makes the circumferential stress in surrounding rock become the main control stress for the roadway deformation and failure. Moreover, the range of PFZ in the roadway roof, floor, roof corner, and floor foot increases gradually, while the range of PFZ in the roadway ribs decreases gradually, resulting in different shapes of PFZ formed in the surrounding rock. All of these suggest that the plastic failure in the region with the polar angle of $30° \leq \theta \leq 150°$ and $210° \leq \theta \leq 330$ is controlled by high geostress, but the plastic failure outside this region is controlled by low geostress.

(3) Under the non-uniformly horizontal geostress, the horizontal lateral pressure coefficient λ_x perpendicular to the axial direction of the roadway is the most important factor affecting the plastic failure of the roadway. With the increase of the horizontal lateral pressure coefficient, the roadway roof and floor become the main plastic failure zones due to the appearance of the large stress and stress-concentration area. Moreover, the greater the ratio of the lateral pressure coefficients in the horizontal x-direction and y-direction, that is, the more obvious the orientation characteristic of the geostress, the more serious the plastic failure of roadway roof, roof corner, floor, and floor foot is, while the relatively smaller the plastic failure of roadway ribs is. Such as, when the lateral pressure coefficient λ_y is 0.5, as the lateral pressure coefficient λ_x increased from 0.5 to 1.5, the range of PFZ in the roadway roof and floor increases by about 12 times.

(4) Based on the engineering geological conditions of the excavating roadway and the directional characteristics of high horizontal geostress obtained from the *in situ* stress test, the range of PFZ and distribution characteristics of PFZ in roadway under the non-uniformly horizontal geostress were obtained by numerical simulation. Based on these features, this paper has proposed a combined support scheme focused on "bolting and shotcreting with wire mesh + deep-shallow coupling full-section bolt-cable-grouting", and refined and optimized the supporting parameters. The field monitored results have shown that the maximum values of the roof-to-floor convergence, rib-to-rib convergence, and separation deformation are 193, 123, and 30 mm, respectively, which are within the safe range. This suggests that the roadway deformation and failure

can be effectively controlled after this combined support was used, to ensure the long-term stability and safety of roadway. Further, these research results provided theoretical foundation as well as methodological reference for the stability control of fractured roadway under deep complex geological structure area and high geostress.

References

[1]   Xie HP, Gao F, Ju Y, Zhang R, Gao MZ, Deng JH. Novel idea and disruptive technologies for the exploration and research of deep earth. Adv Eng Sci. 2017;49:1–8.

[2]   Xie HP. Research framework and anticipated results of deep rock mechanics and mining theory. Adv Eng Sci. 2017;49:1–16.

[3]   Kang HP. Analysis on types and interaction of stress fields in underground coal mines. J Chin Coal Soc. 2008;33:1329–35.

[4]   He FI, Zhang GC. Stability analysis and control of deep under ground roadways subjected to high horizontal tectonic stress. J Chi Uni Min Tech. 2015;44(3):466–76.

[5]   Cao P, Li HY. Instability mechanism and control measures of surrounding rock in deep tunnel under high lateral pressures. Chi J Geo Eng. 2016;38:2262–71.

[6]   Li XP, Wang B, Zhou GL. Research on distribution rule of geostress in deep stratum in Chinese mainland. Chin J Rock Mech Eng. 2012;31:2875–80.

[7]   Liu QS, Liu KD. Characteristics of in-situ stress field for deep levels in Huainan coal mine. Rock Soi Mech. 2012;33:2089–96.

[8]   Liu H, Sang S, Xue J, Wang G, Xu H, Ren B, Liu C, Liu S. Characteristics of an in situ stress field and its control on coal fractures and coal permeability in the Gucheng block, southern Qinshui Basin, China. J Nat Gas Sci Eng. 2016;36:1130–39.

[9]   Park KH, Kim YJ. Analytical solution for a circular opening in an elastic–brittle–plastic rock. Int J Rock Mech Min Sci. 2006;43:616–22.

[10] Sharan S. Elastic–brittle–plastic analysis of circular openings in Hoek–Brown media. Int J Rock Mech Min Sci. 2003;40:817–24.

[11] Sharan S. Analytical solutions for stresses and displacements around a circular opening in a generalized Hoek–Brown rock. Int J Rock Mech Min Sci. 2008;45:78–85.

[12] Fahimifar A, Hedayat AR. Elasto-plastic analysis in conventional tunnelling excavation. Proc Inst Civ Eng Geotech Eng. 2010;163:37–45.

[13] Jiang BS, Zhang Q, He YN, Han LJ. Elastoplastic analysis of cracked surrounding rocks in deep circular openings. Chin J Rock Mech Eng. 2007;26:982–6.

[14] Sun JS, Lu WB. Analytical elastoplastic solutions to supporting rock masses of circular tunnels under asymmetric load. Rock Soi Mech. 2007;28:327–32.

[15] Pan Y, Zhao GM, Meng XR. Elasto-plastic analysis on surrounding rock mass under non-uniform stress field. J Chin Coal Soc. 2011;36:53–7.

[16] Li C, Xu J, Pan J, Ma C. Plastic zone distribution laws and its types of surrounding rock in large-span roadway. Int J Min Sci Technol. 2012;22:23–8.

[17] Ma Q, Tan Y, Zhao Z, Xu Q, Wang J, Ding K. Roadside support schemes numerical simulation and field monitoring of gob-side entry retaining in soft floor and hard roof. Arab J Geosci. 2018;11:563–76.

[18] Hwang RH, Yang TH, Zheng C, Wang PT. Influence of anisotropy on failure mode of tunnel under different lateral pressures. J Uni(Nat Sci) . 2012;33:739–42.

[19] Xiao TQ, Wang XY, Zhang ZG. Stability control of surrounding rocks for a coal roadway in a deep tectonic region. Int J Min Sci Technol. 2014;24:171–6.

[20] Gao F, Stead D, Kang H. Numerical simulation of squeezing failure in a coal mine roadway due to mining-induced stresses. Rock Mech Rock Eng. 2015;48:1635–45.

[21] Yu Y, Bai JB, Wang XY, Shen WL, Lian CJ. Study on asymmetric distortion and failure characteristics and stability control of soft rock roadway. J Min Saf Eng. 2014;31:340–6.

[22] Lin ZB, Yang DF, Li YH. Analysis of the regularity of the displacement and rupture in the circular roadway under different lateral pressure coefficients. J Saf Env. 2017;17:457–62.

[23] Wang F, Zhang C, Wei S, Zhang X, Guo S. Whole section anchor–grouting reinforcement technology and its application in underground roadways with loose and fractured surrounding rock. Tunn Undergr Space Technol. 2016;51:133–43.

[24] Cao R, Cao P, Lin H. Support technology of deep roadway under high stress and its application. Int J Min Sci Technol. 2016;26:787–93.

[25] Zhang JP, Liu LM, Cao JZ, Yan X, Zhang FT. Mechanism and application of concrete-filled steel tubular support in deep and high stress roadway. Constr Build Mater. 2018;186:233–46.

[26] Duan SQ, Feng XT, Jiang Q, Liu GF, Pei SF, Fan YL. In situ observation of failure mechanisms controlled by rock masses with weak interlayer zones in large underground cavern excavations under high geostress. Rock Mech Rock Eng. 2017;50:2465–93.

[27] Feng XT, Pei SF, Jiang Q, Zhou YY, Li SJ, Yao ZB. Deep fracturing of the hard rock surrounding a large underground cavern subjected to high geostress: in situ observation and mechanism analysis. Rock Mech Rock Eng. 2017;50:1–21.

[28] Ge XR, Hou MX. Principle of in-situ 3D rock stress measurement with borehole wall stress relief method and its preliminary applications to determination of in-situ rock stress orientation and magnitude in Jinping hydropower station. Sci China Tech Sc. 2012;55:939–49.

[29] Huang MQ, Wu AX, Wang YM, Bin H. Geostress measurements near fault areas using borehole stress-relief method. Trans Nonferrous Met Soc China. 2014;24:3660–5.

[30] Gu SC, Zhou P, Sun W, Hu C, Li Z, Wang C. Study on the stability of surrounding rock of underground circular cavern based on the anchor reinforcement effect. Adv Civ Eng. 2018;2018:1–18.

[31] Qin D, Wang X, Zhang D, Chen X. Study on surrounding rock-bearing structure and associated control mechanism of deep

soft rock roadway under dynamic pressure. Sustainability. 2019;11:1892.

[32] Xu ZL. Elasticity. 4th ed. Bei Jin: Higher Education Press; 2006.

[33] Carranza-Torres C, Fairhurst C. The elasto-plastic solution of tunnel problems using the generalized form of the hoek-brown failure criterion. Int J Rock Mech Min. 1999;36:777–809.

[34] Yuan C, Wang W, Fan L. Study on distribution law and influencing factors of surrounding rock plastic zone in mining roadway. J Vibroeng. 2019;21:1127–38.

[35] Liu C, Shi W, Liu W, Feng R. Elastic-plastic analysis of surrounding rock in deep roadway considering shear dilatancy property under non-uniform stress field. J Eng Sci Techn Rev. 2017;10:16–24.

[36] Meng QB, Han LJ, Qiao WG, Lin DG, Fan JD. Support technology for mine roadways in extreme weakly cemented strata and its application. Int J Min Sci Technol. 2014;24:157–64.

[37] Yang XJ, Pang JW, Liu DM, Liu Y, Tian YH, Ma J, Li SH. Deformation mechanism of roadways in deep soft rock at Hegang Xing'an Coal Mine. Int J Min Sci Technol. 2013;23:307–12.

[38] Sun YT, Li GC, Zhang JF, Qian DY. Stability control for the rheological roadway by a novel high-efficiency jet grouting technique in deep underground coal mines. Sustainability. 2019;11:6494–500.

[39] Sun YT, Li GC, Zhang JF, Qian DY. Experimental and numerical investigation on a novel support system for controlling roadway deformation in underground coal mines. Energy Sci Eng. 2020;8:490–500.